Polyelectrolyte-protein synergism:
pH-responsive polyelectrolyte/insulin complexes
as versatile carriers for targeted protein and drug delivery

Anastasiia Murmiliuk[1*], Hiroki Iwase[2], Jia-Jhen Kang[1], Shilpa Mohanakumar[3], Marie-Sousai Appavou[1], Kathleen Wood[4], László Almásy[5], Adél Len[5,6], Kuno Schwärzer[7], Jürgen Allgaier[7], Martin Dulle[7], Thomas Gensch[8], Beate Förster[9], Kanae Ito[10], Hiroshi Nakagawa[11], Simone Wiegand[12,13], Stephan Förster[7], Aurel Radulescu[1]

[1] *Jülich Centre for Neutron Science (JCNS) at Heinz Maier-Leibnitz Zentrum (MLZ), Forschungszentrum Jülich GmbH, Lichtenbergstraße 1, 85747 Garching, Germany*

[2] *Neutron Science and Technology Center, Comprehensive Research Organization for Science and Society (CROSS), Tokai, Ibaraki, 319-1106, Japan*

[3] *Physics of Complex Fluids, University of Twente, 7522 NB Enschede, the Netherlands*

[4] *Australian Centre for Neutron Scattering, Australian Nuclear Science and Technology Organization, New Illawarra Road, Lucas Heights, NSW 2234, Australia*

[5] *Neutron Spectroscopy Department, HUN-REN Centre for Energy Research, Konkoly-Thege str. 29-33, 1121 Budapest, Hungary*

[6] *University of Pécs, Faculty of Engineering and Information Technology, Boszorkány str 2., 7624 Pécs, Hungary*

[7] *Jülich Centre for Neutron Science (JCNS-1/IBI-8), Forschungszentrum Jülich, Wilhelm-Johnen-Straße, 52425 Jülich, Germany*

[8] *Institute of Biological Information Processing, IBI-1 (Molecular and Cellular Physiology), Forschungszentrum Jülich, 52425 Jülich, Germany*

[9] *Ernst Ruska-Centre for Microscopy and Spectroscopy with Electrons, Physics of Nanoscale Systems (ER-C-1), Forschungszentrum Jülich, Wilhelm-Johnen-Straße, 52425 Jülich, Germany*

[10] *Industrial Application Division, Spring-8, Japan Synchrotron Radiation Research Institute (JASRI), 1-1-1 Kouto, Sayo, Hyogo 679–5198, Japan*

[11] *Materials Sciences Research Center, Japan Atomic Energy Agency, Tokai, Ibaraki, Japan*

[12] *IBI-4—Biomacromolecular Systems and Processes, Forschungszentrum Jülich GmbH, D-52428 Jülich, Germany*

[13] *Chemistry Department – Physical Chemistry, University Cologne, D-50939, Cologne, Germany*

*E-mail: anastasiia.murmiliuk@gmail.com

Keywords: block polyelectrolyte, protein, insulin, electrostatic co-assembly, core/shell particles, small-angle scattering

ABSTRACT

The co-assembly of polyelectrolytes (PE) with proteins offers a promising approach for designing complex structures with customizable morphologies, charge distribution, and stability for targeted cargo delivery. However, the complexity of protein structure limits our ability to predict the properties of the formed nanoparticles, and our goal is to identify the key triggers of the morphological transition in protein/PE complexes and evaluate their ability to encapsulate multivalent ionic drugs. Oppositely charged polyelectrolyte and protein can assemble into pH-responsive nanoparticles, that destabilize at pH inversion. The additional neutral hydrophilic block should stabilize the particles in solution and allow to use them for encapsulation of a multivalent ionic drug with We demonstrated that diblock copolymers, poly(ethylene oxide)-block-poly(N,N-dimethylaminoethyl methacrylate)polycation and poly(ethylene oxide)-block-poly(N,N,N-trimethylammonioethyl methacrylate), consisting of a polycation block and a neutral hydrophilic block, reversibly co-assemble with insulin in pH range between 5 and 8. Using small-angle neutron and X-ray scattering (SANS, SAXS), we showed that insulin arrangement within formed particles is controlled by intermolecular electrostatic forces between protein molecules, and can be tuned by varying ionic strength. For the first time, we observed by fluorescence spectroscopy that formed protein/PE complexes with excess of positive charges exhibited potential for encapsulating and controlled release of negatively charged bivalent drugs, protoporphyrin-IX and zinc(II) protoporphyrin-IX, enabling the development of nanocarriers for combination therapies with adjustable charge, stability, internal structure, and size.

INTRODUCTION

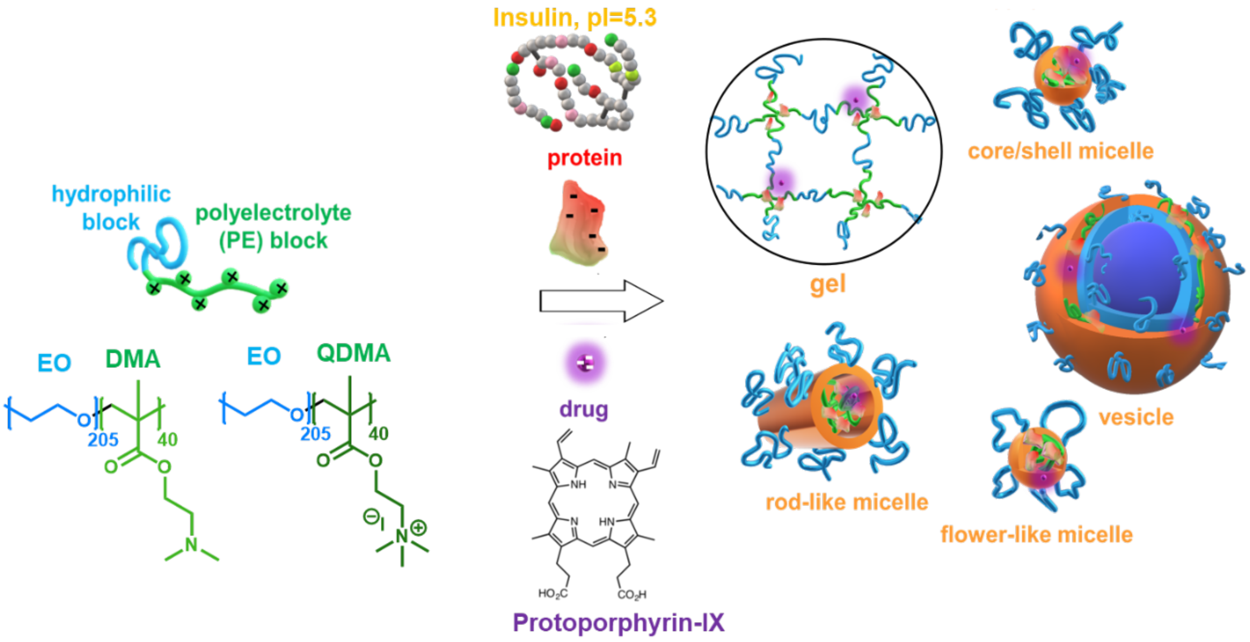

Fig. 1. Schematic representation of polyelectrolyte-protein complex formation and chemical structure of the complex components.

Targeted drug delivery is a therapeutic approach for transporting drugs to specific organs in the body to minimize potential side effects on healthy tissues, enhance the efficacy of the treatments, protect the drug from degradation, and prolong drug release. It is achieved by encapsulation of the drug into a nanoparticle and triggered release. This strategy finds significance in cancer therapy, [1–3] diabetes treatment, cardiovascular disorders, tuberculosis, celiac, or Wilson's diseases. [4] Controlled drug release from nanocapsules can be activated by various stimuli, including pH, reactive oxygen species, glutethimide, or temperature. Nanocarriers, that are designed using biocompatible and biodegradable materials, minimize potential toxicity and ensure safe administration in biological systems. [5] More recently, lipid nanoparticles (LNPs), which consist of a combination of different lipids [6–8] or hybrid nanoparticles of lipidic and polymeric components [9] have been developed and successfully tested for mRNA-based therapies after optimization of molecular organization in correlation with biological activity.

Notably, targeted delivery of proteins plays a crucial role in this concept due to their high enzymatic susceptibility, immunogenic reaction, and short shelf life. [10,11] Exploiting the zwitterionic properties of proteins (the sign of protein total charge is controlled by pH) enables the formation of pH-responsive complexes with oppositely charged species, for instance polyelectrolytes or other proteins, that could be used for protein encapsulation and controlled release. [12] The ability to respond to changes in pH enables these nanocarriers to selectively release drugs or therapeutic agents at specific sites, such as tumor tissues or inflamed areas, where pH is different from the surrounding healthy tissues. In addition, pH-responsive nanocarriers provide precise control over kinetics of drug release, allowing for sustained release or triggered release in response to pH variations, by that optimizing therapeutic outcomes and diminishing side effects. Such an approach is particularly vital for insulin delivery in diabetic patients with allergic reactions or for achieving a slow, gradual release of the protein. Incorporating insulin into targeted drug delivery systems can protect insulin from enzymatic degradation and enhance its stability during storage and transit. Previous studies have demonstrated the efficiency of insulin/polyelectrolyte complexes, in particular Pippa and co-workers have shown the complex formation of insulin and cationic quaternized poly[3,5-bis(dimethylaminomethylene)hydroxystyrene]-block-poly(ethylene oxide), QNPHOS-EO, in aqueous solution and in biological medium, and demonstrated preservation of the native structure of insulin in the complexes and the possibility of fast insulin release. [13] Mao and co-workers have observed that co-assembly of insulin with chitosan derivatives significantly increases the stability of insulin even at high temperature or particle lyophilization. [14] However, internal structure of such complexes, aggregation behavior of insulin in the complex and after release, as well as detailed study of the PE and insulin ionization still need to be explored, since they have significant impact on encapsulation efficiency, complex stability, biological activity and controlled release of insulin. Furthermore, the charge of the polyelectrolyte/insulin complexes could be controlled by variation of the ratios of charged groups, rendering them suitable for targeted delivery of multivalent low-molar mass drugs and potentially for combination therapies. Similarly to mRNA delivery systems that were studied earlier in our group, formed complexes are expected to be of nanometer size particles with packed negatively charged biomacromolecules inside and multilayer structure, so that we can use apply acquired knowledge about protein systems for design more complex delivery system with higher number of components.

This research investigates the morphology and controlled release potential of insulin/polyelectrolyte complexes, shedding light on their suitability for advancing targeted drug delivery systems. In our work, we studied the complexation of insulin with a biocompatible diblock copolymer consisting of a weak polycation poly(N,N-dimethylaminoethyl methacrylate), DMA, or a strong polycation poly(N,N,N-trimethylammonioethyl methacrylate), QDMA, and a neutral hydrophilic poly(ethylene oxide), EO, block at physiological pH (see Fig. 1). The presence of weak charged functional groups allows us to control the stability and morphology of the complex, and thus encapsulation properties by variation of the polymer and insulin charge. We followed the co-assembly of PE and insulin and their disassembly using calorimetry, scattering, and microscopy. The novelty of our approach comes from the possibility to encapsulate not only insulin but also negatively charged moieties. The formed complexes were used for encapsulation and release of bivalent negatively charged low-molar mass drug, protoporphyrin-IX, PrP, and zinc (II) protoporphyrin-IX, ZnPrP, that are used as photosensitizers for photodynamic therapy in cancer treatment due to their ability to generate reactive molecular species in the presence of oxygen and light, and thus destroy cancer cells.

RESULTS & DISCUSSION

1. Conformation and charge regulation in weak and strong polyelectrolytes

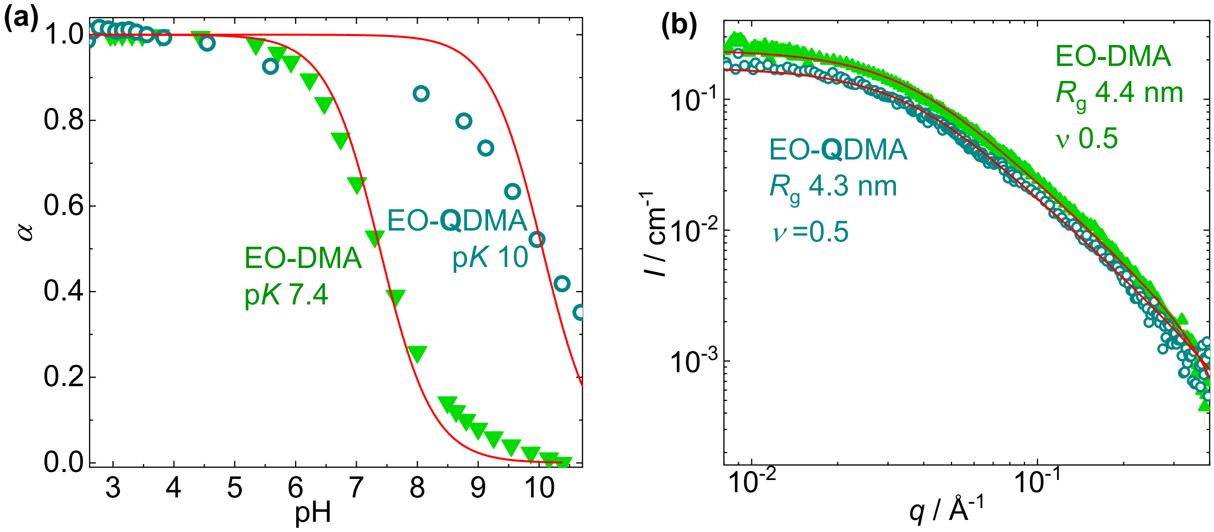

Fig. 2. (a) Degree of ionization, *α*, of strong EO-QDMA and weak EO-DMA polyelectrolytes calculated from potentiometric titration using electroneutrality equation (eq. S2); red lines are the ideal titration curves for p*K* 7.4 and 10 obtained from Henderson–Hasselbalch equation (eq. S3). **(b)** SANS curves of EO-DMA and EO-QDMA at pH 7.5 in 50 mM NaCl and polymer concentration 5g/l fitted with the generalized Gaussian Chain model (red lines).

To design pH-responsive nanocapsules based on pH-responsive materials, a comprehensive understanding of the dynamics and morphology of these materials is crucial. In contrast to a strong polycation QDMA, the ionization of a weak polycation DMA is highly pH sensitive. The potentiometric titration of the block copolymers with a strong or a weak PE allows us to calculate their degrees of ionization as a function of pH (see Fig. 2a). The p*K* value of EO-DMA, obtained from titration curve, is equal to 7.4, indicating that at physiological pH the degree of ionization is 0.5 and only half of the amine groups of DMA bear positive charge. EO-DMA copolymer is fully charged at pH below 6, and not charged at pH above 9. In contrast, strong PE is charged in the whole pH range, has p*K* of 10, and at physiological pH has 90% of groups positively charged. By comparing the behavior of a weak and strong PE in the complexes with proteins, we can gain insights into the impact of PE ionization on the co-assembly process with proteins.

Despite the significant difference in chain length of the PE block (40 monomeric units) and the neutral EO block (205 monomeric units), the repulsion between like charges can still exert an influence on the conformation of the block copolymer. Fig.2b shows small-angle neutron scattering (SANS) profiles of strong EO-QDMA and weak EO-DMA polyelectrolytes. At pH 7.5, no significant difference in scattering profiles of strong and weak PEs was observed. SANS curves were fitted using generalized Gaussian coil model (see section 4.4.2 in the Supporting Information), and similar gyration radii, R_g, of 4 nm and Flory exponent, ν=0.5, confirm predominant contribution of EO block to the general conformation of the block copolymer.

Investigation of pH-responsiveness of the polymers using SANS (see Fig. S3 in Supporting Info) revealed the conformational change to more compact coil of weak EO-DMA at high pH, resulting in a "bell-shaped" peak at low q in the Kratky plot, whereas for strong PE no significant change in scattering profile is observed. The diffusion coefficient, D, as determined by dynamic light scattering (DLS), exhibits an increase at high pH for weak PE (see Fig. S5). This effect can be attributed to the decrease in PE ionization, weakening of the repulsion between like-charged groups and increased hydrophobicity of the chain. It results in the collapse of the PE block at pH 9, driven by hydrophobic interaction, more compact conformation of polymer chain and faster diffusion. Additionally, the loss of the double electric layer of counter ions, that diffuse in solution together with PE, also contributes to the increase in the diffusion coefficient.

2. Insulin aggregation in aqueous solution

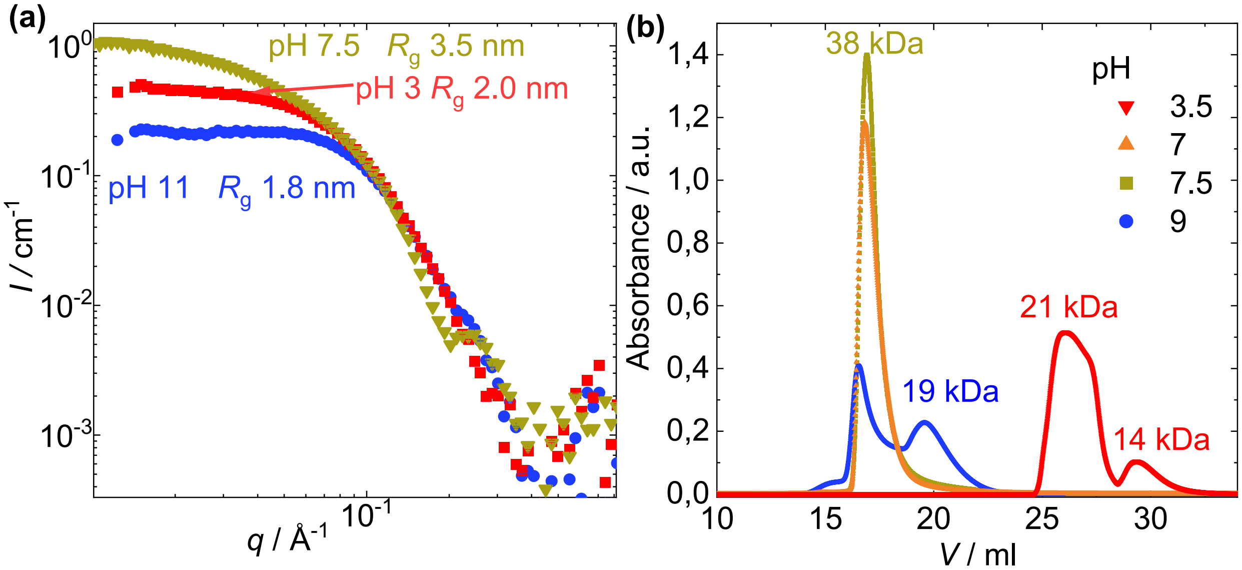

Fig. 3. (a) SANS curves of insulin oligomers at various pH and insulin concentration 20 g/l. **(b)** UV signal of insulin after SEC at wavelength, λ, 280 nm. The values of Mw were obtained from multi-angle light scattering experiment. The UV signal of insulin at pH 3 is shifted to higher elution volume due to the different calibration.

It has been shown that insulin can exist in different oligomeric state depending on pH, salt concentration and buffer. [15] Given that the biological effectiveness of insulin relies on the nature of oligomers, it became crucial in our research to analyse the insulin aggregation under different conditions. Using SANS and size exclusion chromatography (SEC), we showed that the aggregate state of human insulin in 50 mM NaCl solution is hexamer, trimer, or dimer (see Fig. 3). The type of oligomer was estimated from the molecular weight, M_W, of insulin, calculated using multi-angle light scattering (MALS) measurement after SEC experiment and considering M_W of insulin monomers equal to 5.8 kDa (see section S3.2 in the Supporting Information). At pH 7.5, insulin forms predominantly hexamers with a globular shape and R_g of 3.5 nm, while at pH 9 there is an equilibrium between hexamers and trimers, and at pH 3 there is an equilibrium between trimers and dimers with the apparent R_g of 2 nm (Fig. S6a). The SANS curves of insulin at pH 3 and 11 in low q range are affected by strong electrostatic repulsion between charge particles, that was confirmed by fitting the curves using Ellipsoidal model with Schultz-Zimm distribution and Hayter-Penfold structure factor (see section S3.1 and Fig. S6b in the Supporting Information). The difference in aggregation behaviour of insulin could be explained by different charge and ionization degree of protein at various pH, which affects intermolecular electrostatic and hydrophobic interaction. It is worth mentioning that in the pH range between 4 and 7, insulin has limited solubility, and we observed precipitation of the protein, therefore some of the experiments for characterization of insulin cannot be reliably analyzed in this pH range. However, at pH below 4 insulin is fully soluble in water.

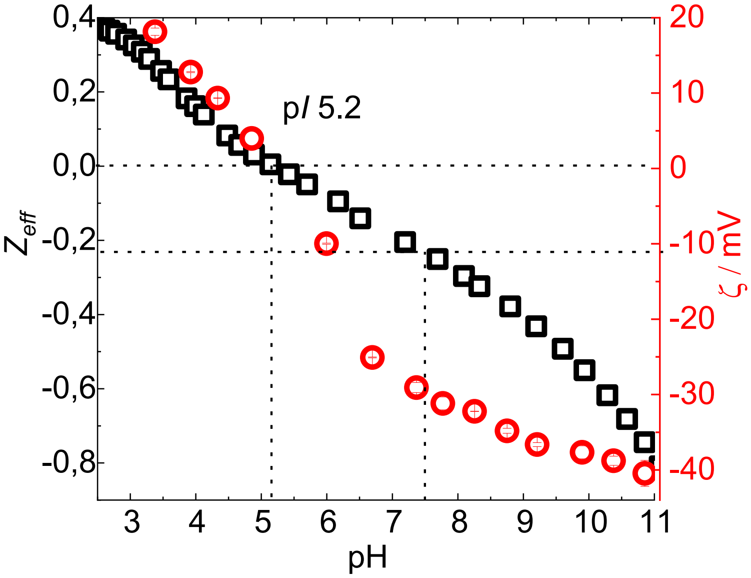

Fig. 4. Effective charge, Z_{eff}, obtained from potentiometric titration using electroneutrality equation (eq. S2), (black squares) and zeta-potential, *ζ*, (red circles) of insulin as a function of pH.

Since insulin possesses amino acids containing positively and negatively charged ionizable groups, the overall charge of the protein can be varied by pH changes. The experimental isoelectric point, p*I,* value of human insulin 5.2, calculated from potentiometric titration measurement, agrees with literature data [16] and ζ-potential experiment (see Fig. 4). At pH 3 and 9, insulin is highly charged, with effective charge, *Z*, of 0.4 and -0.4, and zeta-potential, *ζ*, of +18 and -35, respectively. The patchy charge distribution within insulin molecules increases the intermolecular repulsion so that the formation of smaller aggregates is more favourable. On the contrary, at pH closer to p*I* of insulin, the absolute value of the protein total charge decreases, and the repulsion between protein molecules decreases, which triggers subsequent protein aggregation.

3. Polyelectrolyte/protein complexes

3.1 Particle formation and morphology

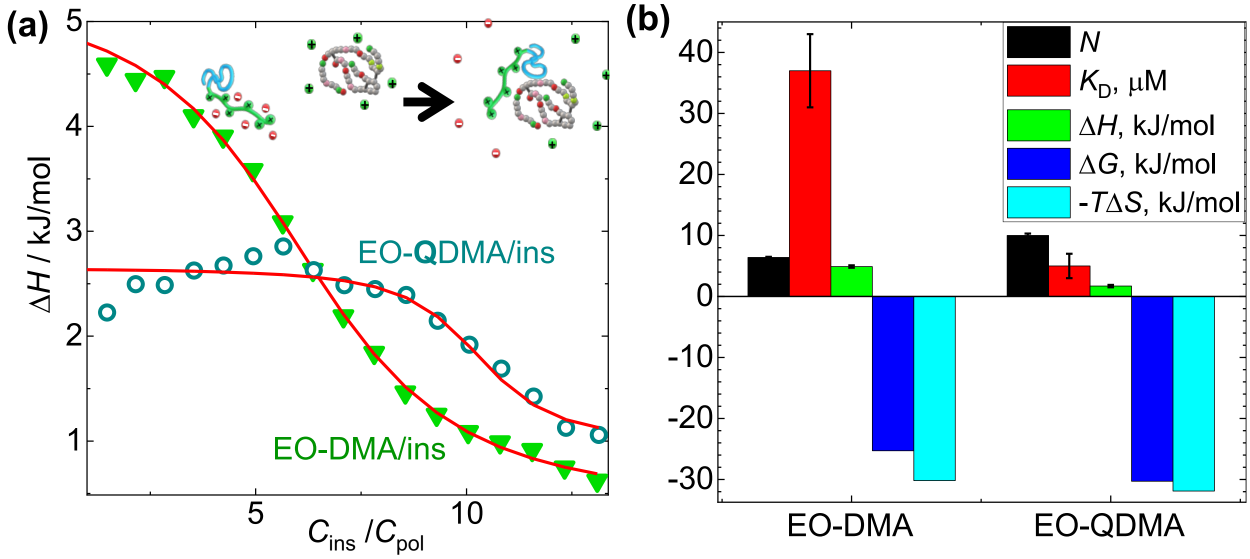

Fig. 5. (a) Integrated titration curves from ITC of insulin titrated into 5 g/l solution of EO-DMA or EO-QDMA at pH 7.5 in 50 mM NaCl. **(b)** Thermodynamic parameters (stoichiometry coefficient, *N*; dissociation constant, K_D; enthalpy, Δ*H*; Gibbs energy, Δ*G*; and entropy, *T*Δ*S*) calculated by fitting the titration curves by one-set-of-site model.

Mixing EO-DMA or EO-QDMA with insulin at pH 7.5 leads to formation of observable particles, evident from the reduced solution transparency (see Fig. S8). To gain insight into the driving force behind this complex formation and explore its thermodynamics, we conducted isothermal titration calorimetry (ITC) experiments by titrating insulin into the polymer solution at pH 7.5. Fig. 5 presents the integrated titration curves for weak and strong PE along with the thermodynamic parameters obtained by fitting the curves using one-set-of-site model, which assumes the existence of a single binding site for the 'ligand', [17] since binding isotherms of EO-DMA and EO-QDMA with insulin have one sigmoidal profile. Partial differentiations in binding affinities are negligible and thermodynamic parameters, obtained from fitting with one-set-of-site model, are averaged values over possible deviations. The dissociation constant, K_D, of the complexes with weak PE, EO-DMA, is ca. 7 times higher than for strong PE, EO-QDMA (37 ± 6 μM and 5 ± 2 μM, respectively) due to the lower energy of electrostatic attraction between polymer and insulin, and longer distance between oppositely charged molecules. At the same time stoichiometry of complex formation, *N*, is 1.6 times higher for EO-QDMA (10 ± 0.3, in comparison to *N* of EO-DMA 6.4 ± 0.1), confirming the presence of 1.5 times higher amount of positive charged groups available for complexation with insulin in comparison with weak PE. Furthermore, the results of our ITC experiments revealed that for both PE, the complex formation is enthalpy unfavourable, Δ*H* is 4.9 ± 0.2 kJ/mol for EO-DMA and 1.7 ± 0.2 kJ/mol for EO-QDMA. In addition, the contribution of entropy outweighs the enthalpy, indicating that the process of PE-insulin co-assembly is primarily driven by entropy. This phenomenon is attributed to the release of counter-ions and water molecules from hydration shell of insulin and PE, signifying that the driving force for complex formation is the electrostatic attraction between oppositely charged groups. [18–20] Consequently, the complex formation, stability, and properties of the PE-insulin assembly can be controlled by affecting electrostatic interactions through charge regulation and charge screening.

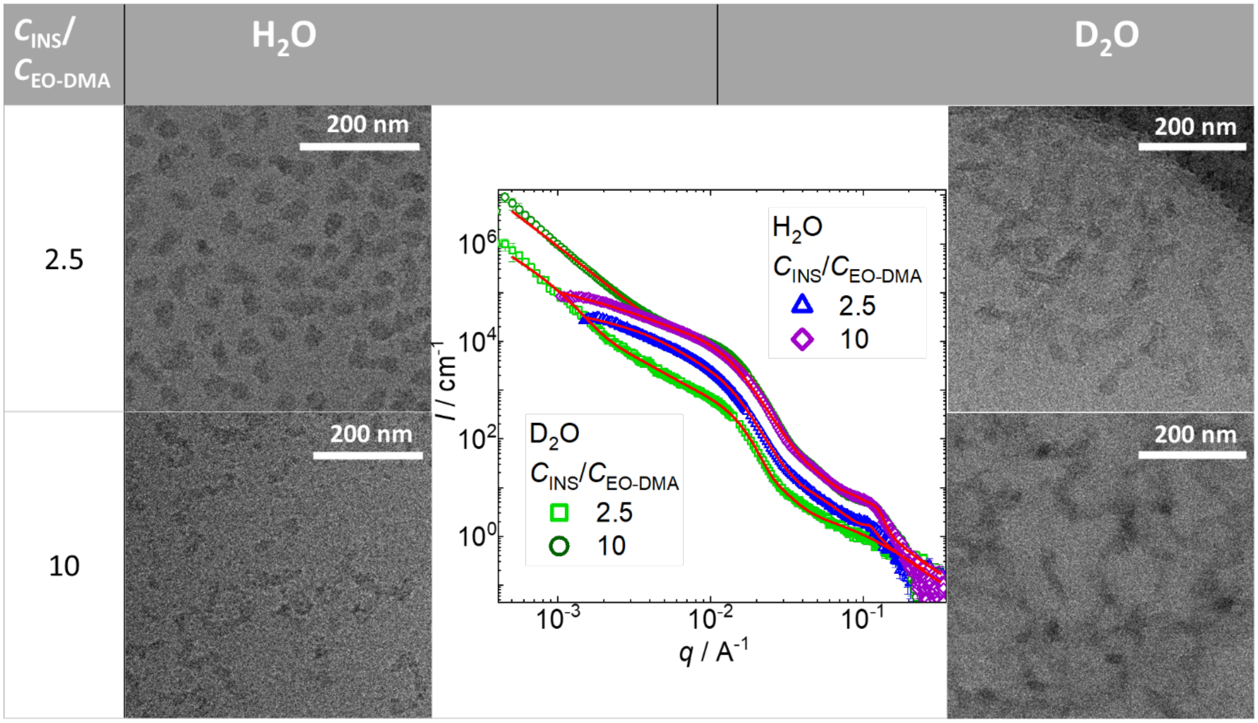

Fig. 6. Cryo-TEM micrographs and USAXS curves for EO-DMA complexes with insulin at different insulin concentration, C_{INS}, in H_2O and D_2O in 50 mM NaCl. Red lines are fitting curves obtained using the model of a Sphere with Gaussian chains attached, Schulz-Zimm distribution of the sphere radii, and Broad Peak model to fit correlation peak, and Extended Guinier Law model to fit upturn at low *q*.

Fig. 6 shows the morphology of the complexes in aqueous solution. At $C_{INS}/C_{EO\text{-}DMA}$ 2.5, polymer with insulin in H_2O forms spherical and elongated particles with average size of 40 ± 15 nm. At higher insulin concentration, elongated and worm-like particles are formed. At the same time the complexes in D_2O form a network of interconnected particles. Similar features are observed in ultra small-angle X-ray and neutron scattering (USAXS, USANS) curves (Fig. 6 and Fig. S17) for samples in deuterated solvent, where the upturn appears at low *q*, while the mid-*q* profiles (4×10^{-3} – 0.3 Å^{-1}) remain the same. This effect could be attributed to different conformational behavior of EO block in D_2O, in comparison to H_2O, due to the stronger hydrogen bonding between D_2O molecules, and, therefore, weaker hydrogen bonding between EO and D_2O, and stronger inter- and intramolecular hydrogen bonding between EO segments. [21–23] As a result, intramolecular interaction of EO blocks leads to agglomeration of polymer/insulin complexes and formation of a network in solution, while the internal structure of the complexes does not change. In contrast, complexes prepared in H_2O have a Guinier regime at q below 0.003 Å^{-1}, corresponding to the particles with R_g 58 ± 5 nm, indicating the presence of particles with well-defined size.

The hydrodynamic diameter, D_H, of the EO-DMA/ins particles, calculated from DLS measurement, rises to 233 nm at $C_{INS}/C_{EO\text{-}DMA}$ equal to 1 (Fig. S9), and slightly decreases at higher insulin concentrations due to the multiple scattering. ζ of the complexes is positive up to insulin-to-polymer ratio of 1, and the charges of DMA groups are compensated with negatively charged insulin molecules at the ratio between 1 and 2, that is supported by matching SAXS profiles of the complexes in the mid-q range at $C_{INS}/C_{EO\text{-}DMA} > 2$ (Fig. 7a). Variation of the insulin concentration in SAXS experiments demonstrated rise in scattering intensity with increasing C_{INS} due to the increase in the number of particles. When the insulin-to-polymer ratio surpasses 1, the correlation peak at q 0.11 Å $^{-1}$ emerges and becomes more pronounced at higher insulin concentrations, indicating an internal arrangement within the complexes. The correlation peak position is related to correlation distance between arranged segments, d_C, via equation $q=2\pi/d_C$, that is equal to 6 nm. However, more detailed investigation of internal structure of the complexes is unreliable in SAXS due to the small difference in scattering lengths for polymer blocks and protein. On the contrary, contrasts in SANS experiments could be varied by solvent composition, in particular H_2O-to-D_2O ratio, or by deuteration of polymeric blocks.

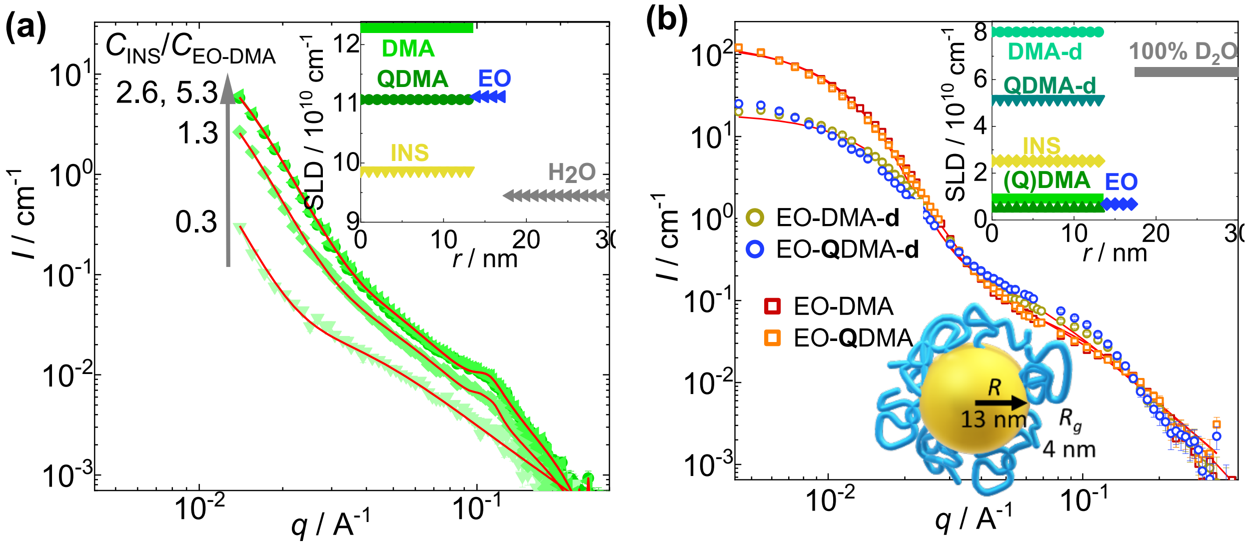

Fig. 7. **(a)** SAXS curves of EO-DMA/insulin complexes at different insulin concentration (curves for $C_{INS}/C_{EO\text{-}DMA}$ 2.6 and 5.3 overlap) in 50 mM NaCl H_2O, and **(b)** SANS curves for the polymer/insulin complexes at $C_{INS}/C_{EO\text{-}DMA}$=10 in 50 mM NaCl D_2O. Inset: calculated SLD values of insulin and DMA, DMA-d, QDMA, QDMA-d and EO blocks for X-rays and neutrons. All

curves are fitted with a model of Sphere with attached Gaussian chains, Schulz-Zimm distribution of the sphere radii, and Broad Peak model to fit correlation peak (red lines).

Fig. 7b shows SANS curves of insulin complexes with weak and strong PE with protonated or deuterated DMA block at $C_{INS}/C_{EO\text{-}DMA}$=10 and theoretical scattering length densities (SLD). Due to the small difference in contrasts of fully protonated polymers (EO-DMA, EO-QDMA) and insulin in 100% D_2O, no correlation peak is visible on the SANS curves, while for deuterated polymers (DMA-d, QDMA-d) the correlation peak emerges for both weak and strong PE exhibiting comparable intensity, because their SLD values are significantly different compared to insulin and EO block, aligning closely with SLD of D_2O. The finding confirms that contrast variation can help in revealing internal features of the complexes.

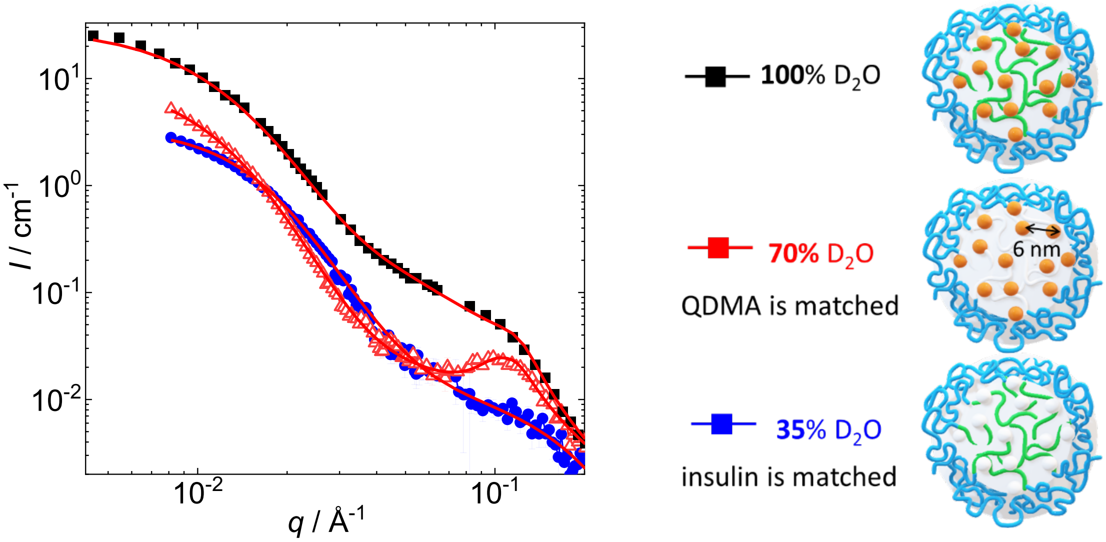

Fig. 8. SANS curves for EO-QDMA-d/insulin complexes at $C_{INS}/C_{EO\text{-}QDMA\text{-}d}$=10 with contrast matching measured in 100%, 70% and 35% D_2O in 50 mM NaCl, and schematic representation of the particle structure – core/shell with the core composed of QDMA block (green chains) and insulin (orange circles) surrounded by EO shell (blue chains). All curves are fitted with a model of Sphere with attached Gaussian chains, Schulz-Zimm distribution of the sphere radii, and Broad Peak model (red lines).

SANS and SAXS curves were fitted using the model of a hard sphere with attached Gaussian chains, see eq. 1, where form factor $P(q)$ consists of self-correlation of the sphere, self-correlation of the chains, cross-correlation between the chains and cross-correlation of between the sphere and the chains.

$$P(q) = 9N_{agg}^2\rho_s^2\left[\frac{\sin(qR)-qRcos(qR)}{(qR)^3}\right]^2 + 2N_{agg}\rho_c^2\frac{\exp(-r_g^2q^2)-1+r_g^2q^2}{r_g^4q^4} + \quad +N_{agg}(N_{agg} - 1)\rho_c^2\left[\frac{1-\exp(-r_g^2q^2)}{r_g^2q^2}\right]^2\left[\frac{\sin(qR+qdr_g)}{qR+qdr_g}\right]^2 + +6N_{agg}^2\rho_s\rho_c\left[\frac{1-\exp(-r_g^2q^2)}{r_g^2q^2}\right]\left[\frac{\sin(qR)-qRcos(qR)}{(qR)^3}\right]\left[\frac{\sin(qR+qdr_g)}{qR+qdr_g}\right] \tag{1}$$

where N_{agg} is the aggregation number, R is the sphere radius, ρ_s is the total excess scattering length of sphere, Rg is the root-mean-square radius of gyration of a chain, and ρ_c is the total excess scattering length of a single chain, and non-penetrating of the chains into the core region is mimicked by $d = 1$ for $R >> R$g. The polydispersity of core radius was included using Schulz-Zimm distribution, and the correlation peak at q 0.1 Å^{-1} that appears for the complexes with high insulin concentration was fitted using Broad Peak model (see the description of the models in Supporting Information, section S4.4.2).

Fitting the SANS curves with the model of Sphere with Gaussian Chains attached revealed that the EO-DMA/insulin complexes consist of spherical core with 13 nm radius surrounded by an outer shell with Rg of polymer chains 4 nm (see fitting parameters in the Table S2 and Table S3). However, the internal structure of the complexes and the origin of the correlation peak remained unclear. To reveal the structure of the particles, we performed contrast variation for SANS by changing H_2O-to-D_2O ratio of solvent. At 70 % D_2O PE block of EO-QDMA-d is fully matched and the scattering comes only from EO block and insulin, the correlation peak at q 0.11 Å^{-1} becomes well-pronounced, while the scattering from large particles is still visible. At 35 % D_2O the neutron scattering from insulin is matched, and only QDMA-d and EO blocks are visible to neutrons. In these conditions, the correlation peak disappears, and the scattering profile at low q remains similar. These two observations indicate the ordering of insulin molecules within the core of the particle formed by QDMA-d/insulin and surrounded by EO outer shell.

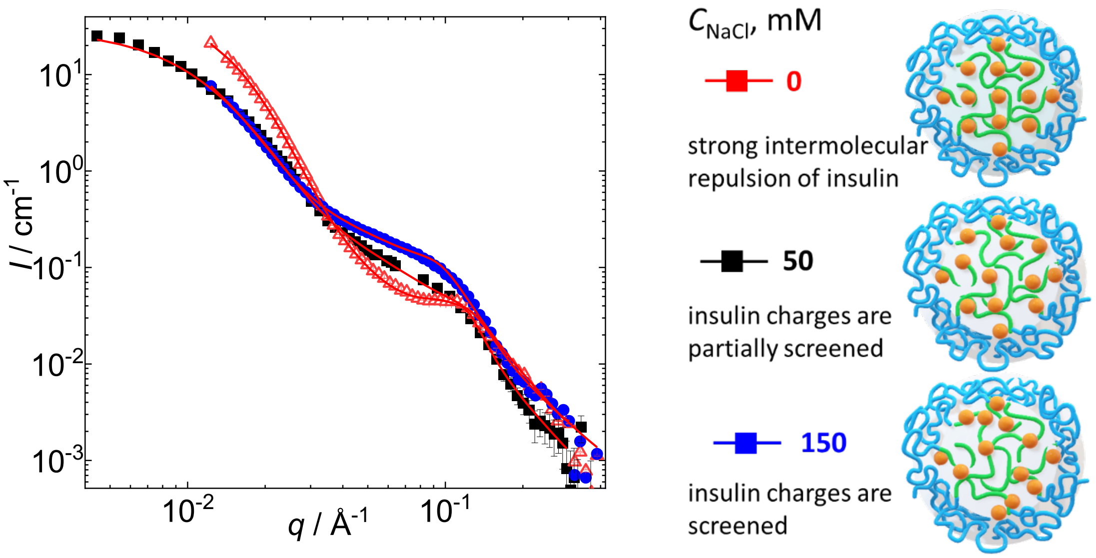

Fig. 9. Salt effect on insulin encapsulation into EO-QDMA-d/insulin complexes $C_{INS}/C_{EO\text{-}QDMA\text{-}d}$=10. SANS curves for the complexes were prepared at sodium chloride concentration, C_{NaCl}, 0, 50 and 150 mM in 100% D_2O. The curves are fitted with a model of Sphere with attached Gaussian chains, Schulz-Zimm distribution of the sphere radii, and Broad Peak model (red lines).

Since the main driving force for complex formation is electrostatic attraction between oppositely charged EO-DMA and insulin, ionic strength of the solution should have significant effect on complex formation and morphology. The SANS experiments for the complexes at different concentration of sodium chloride, C_{NaCl}, (Fig. 9) show the effect of ionic strength on the internal structure of the complexes. In the presence of salt, 50 and 150 mM NaCl solution, SANS curves for EO-QDMA-d/insulin complexes in 100 % D_2O have a broad peak at q 0.1 $Å^{-1}$, while in the absence of salt, the correlation peak is well pronounced even though QDMA-d block is not fully matched. An even stronger change in the peak position and width was observed at 70% D_2O (Fig. S14). Evidently, the arrangement of insulin molecules within the particle core is affected by intermolecular electrostatic repulsion caused by the patchy charge distribution in proteins. [24] At high ionic strength, the charges on insulin are screened from each other, diminishing the degree of protein arrangement, and broadening the correlation peak. It results in insulin molecules being more densely packed, leading to a reduction in the size of the complexes and the forward scattering compared to those prepared without salt.

3.2 pH-responsiveness of the complexes

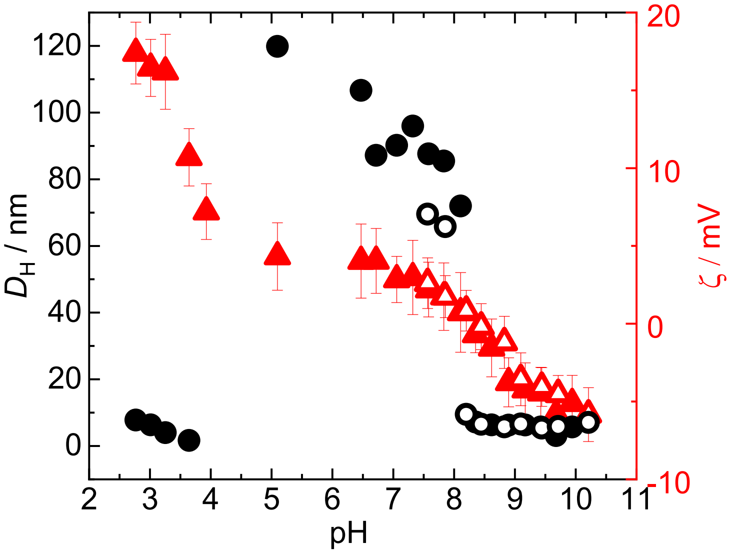

Fig. 10. Number weighted hydrodynamic diameter, D_H, and zeta potential, ζ, of EO-DMA/insulin complex titrated from pH 7.5 to 10 (full symbols) and back down to pH 3 (empty symbols) at C_{INS}/C_{PE}=0.5 in 50 mM NaCl.

The involvement of proteins and PE into the development of nanocarriers was driven by the opportunity to manage their properties and stability via pH modifications. Consequently, we examined the complexes' sensitivity to variations in pH. The examination of complex stability in whole pH range was performed using dynamic and electrophoretic light scattering (DLS, ELS), see Fig. 10 and S15. The scattering intensity is low at pH above 8.4 and below 3.3 indicating absence of the complexes in this pH range, while at $3.3 < pH < 8.4$ the scattering intensity increases 10 times due to the formation of particles with the size D_H 86 ± 7 nm. Fig. 10 shows that the complexation is reversible, and the particles with similar size and ζ are formed even after their disruption at pH above 8.4.

The disruption of complexes is also confirmed by SANS data. At pH 7.5, stable complexes are formed by EO-DMA and insulin, as was described above, and they remain in solution at pH 8 (Fig. 11a). Further increase in pH to 11 leads to decrease in forward scattering by two orders of magnitude due to the complex disruption, caused by significant decrease in ionization of the polymer ($\alpha_{\text{EO-DMA}}$ is 0). At this pH, free polymer chains and insulin aggregates are dissolved in solution, that is confirmed by the fitting parameters using Ellipsoid and Gaussian chain models. The curve fitting resulted in the same sizes of the protein and polymeric chain as for the pure insulin or polymer solutions. Lowering pH to the value below p*I* of insulin, leads to disruption of the complexes as well due to the insulin charge inversion to positive values (at pH 3 *Z* of insulin is 0.4 and ζ is +18 mV).

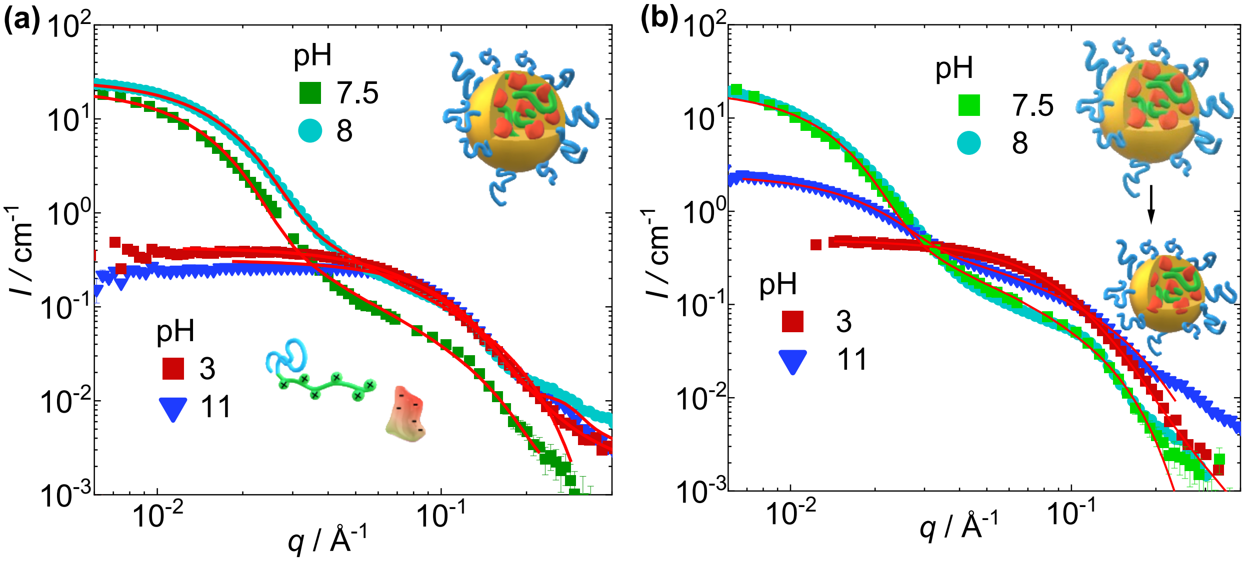

Fig. 11. pH-responsiveness of the complexes in 50 mM NaCl 100 % D_2O at $C_{\text{INS}}/C_{\text{PE}}$=10 formed by (a) weak PE, EO-DMA-d, and (b) strong PE, EO-QDMA-d. The red curves are fitting curves using the model of Sphere with Gaussian Chains attached or Ellipsoid and Gaussian coil.

On contrary, Fig.11b demonstrates that for strong EO-QDMA there is no significant change in SANS curves for the complexes with insulin at pH 7.5 and 8, because the charge of EO-QDMA changes negligibly (0.88 at pH 7.5 and 0.86 at pH 8), and, therefore, electrostatic interaction between polymeric chains and protein molecules in the complex is not affected. At pH 11 the complex remains stable, since polymer and insulin remain charged, while the core radius, *R*, decreases to 7 nm. Stronger electrostatic attraction between EO-QDMA and insulin, due to more negative charge of insulin *Z* -0.6 and ζ -35 and more effective charge neutralization, causes formation of compact core of the complex. Lowering pH to 3 results in the inversion of insulin charge and complexes disruption. Therefore, simple polymer modification of weak PE into strong

PE allowed us to modify the pH range of complex stability, that can be advantageous in targeted delivery applications.

The complete encapsulation of insulin molecules into the complexes was also observed from UV-signal of insulin in SEC (Fig. 12). At wavelength, λ, 280 nm, UV-signal of EO-DMA (integral intensity, $I_{\text{EO-DMA}}$, is 0.05 a.u., see Fig. S20b) is negligible in comparison to the signal from insulin (I_{INS} 1.14 a.u.), therefore, it is reasonable to assume that the UV signal in EO-DMA/insulin mixture primarily originates from insulin. At pH 7.5, the complex is formed, and all insulin molecules are involved into large particles with M_{w} above 150 kDa. After pH increase and complex disruption, insulin molecules are released in the solution as trimers (M_{W} ca. 17 kDa) and hexamers (M_{W} ca. 30 kDa). However, almost equal proportion of hexamers and trimers exist in solution (1.1:1.0), in contrast to ca. double excess of hexamers in the solution of pure insulin at pH 9 (1.8:1.0). This suggest that insulin predominantly exist as trimer within the EO-DMA/insulin particles. The same system measured after 1 day shows the shift in the equilibrium between hexamers and trimers to more stable hexameric form for both pure insulin and EO-DMA/insulin complexes (Fig. S20a). Notably, the USANS experiment for the EO-DMA/insulin complexes in D_2O demonstrates the presence of the large aggregates even at pH 11 (Fig. S17), confirming the assumption that D_2O as a solvent enhances intermolecular interaction within EO block. [22,23]

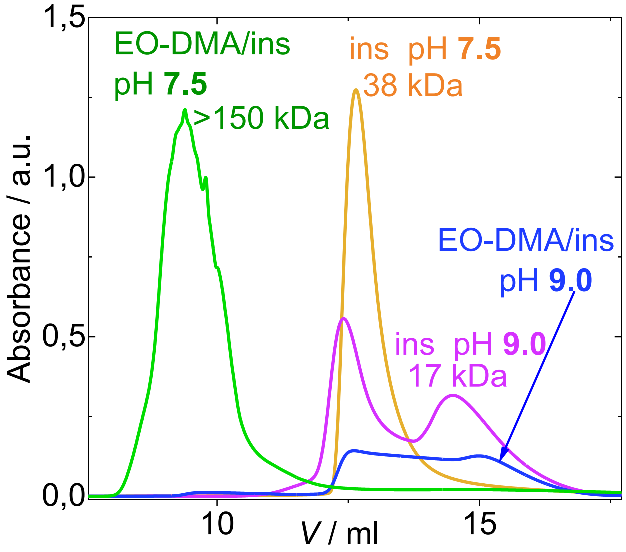

Fig. 12. SEC-UV of insulin and EO-DMA/insulin at $C_{\text{INS}}/C_{\text{EO-DMA}}$=10 at pH 7.5 and 9 in 50 mM NaCl-13mM Tris buffer measured at λ 280 nm. M_{W} was obtained by calibration using a mixture of proteins with known M_{W} as well as using MALS, Fig. S19.

4. Drug encapsulation into the polymer/insulin complexes and controlled release

An excess of positively charged groups within polymer/insulin particles occurs ($\zeta > 0$, see Fig. S9) when the mass concentration of insulin, C_{INS}, is less than double the polymer concentration, $C_{\mathrm{EO\text{-}DMA}}$ or $C_{\mathrm{EO\text{-}QDMA}}$. Therefore, at this insulin-to-polymer ratio, encapsulation of negatively charged multivalent drug into such complexes is driven by increase in entropy of the system due to the counterion release. In this work, we followed encapsulation and release of a fluorophore protoporphyrin-IX (PrP) with 2 carboxyl groups that are negatively charged at pH above 7. [25,26] The integral fluorescence emission intensity of PrP, I_{total}, and the intensity of the PrP characteristic peak at λ 678 nm, I_{678}, increased dramatically after addition of polymer/ins (2.9 times for EO-DMA, and 4.3 times for EO-QDMA, see Fig. 13 and Table S4) in comparison to free PrP, indicating higher solubility of PrP or formation of different type of aggregates with higher quantum yield in the environment of polyelectrolyte complexes.

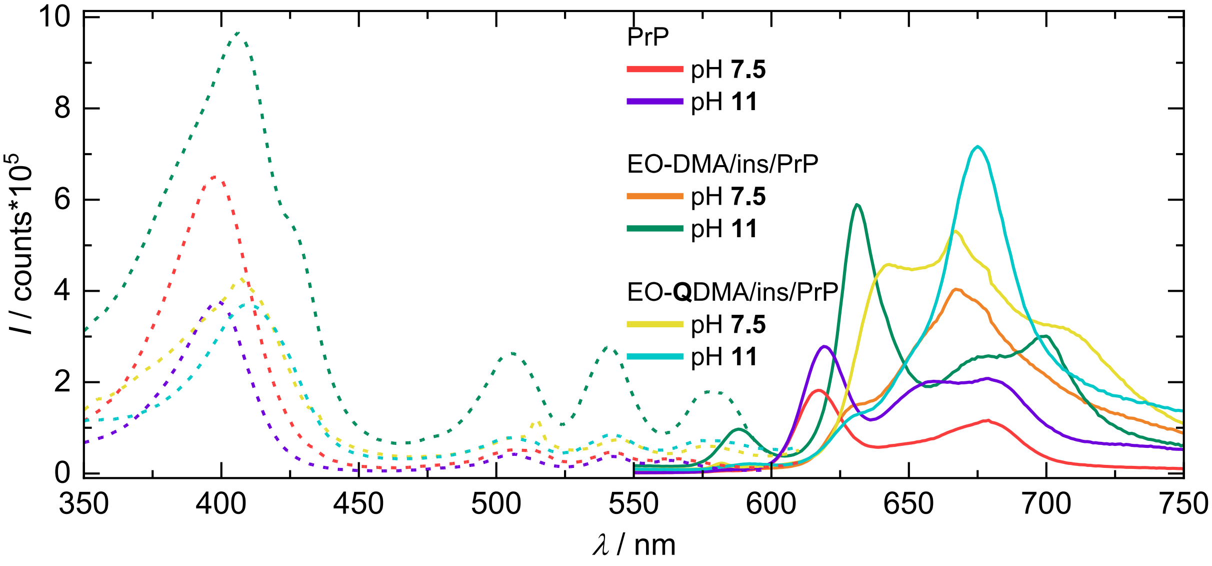

Fig. 13. Fluorescence excitation and emission spectra of PrP before and after encapsulation into polymer/insulin complexes at $C_{\mathrm{INS}}/C_{\mathrm{EO\text{-}QDMA\text{-}d}}$=0.5 in 50 mM NaCl at pH 7.5 and 11, measured at emission wavelength, λ_{EM}, 630 nm and excitation wavelength, λ_{EX}, 375 nm.

By measuring fluorescence decay of both free PrP in solution and in the complex (see Fig. S23), the encapsulated and free fluorophore can be differentiated based on their fluorescence lifetimes, τ. The lifetimes of PrP were determined by fitting decays using a double exponential function, resulting in two distinct lifetimes at each pH value (see Table 1). The shorter lifetime, τ_2, is indicative from aggregates, while the longer component, τ_1, is associated with monomers of PrP. [27] Notably, τ_2 is invariable after complex addition or pH variation, and the encapsulation has a limited impact on quenching of the fluorescence of PrP aggregates. However, both pH variation and encapsulation result in additional fast lifetime component, τ_3, indicating formation of large PrP aggregates induced by change of fluorophore environment. The long lifetime τ_1 of free PrP decreases from 15 ns to 14 ns at higher pH due to the alteration in electrostatic interactions between PrP molecules. The reduction in τ_1 to 12 ns observed after mixing of PrP with EO-DMA/ins or EO-QDMA/insulin complexes at pH 7.5 can be attributed to substantial fluorescence quenching resulting from encapsulation of PrP monomers into the complexes and the electrostatic attraction of negatively charged fluorophore by positively charged groups within the complex. At pH 11, EO-DMA/insulin complexes disassemble, leading to the release of PrP from the particles accompanied by τ_1 increase similar to lifetime of free PrP. In contrast, when the fluorophore is encapsulated into the EO-QDMA/ins complexes, it is not released upon pH change. Instead, it binds even stronger to the complex, that enhances fluorescence quenching and results in further reduction of τ_1 to 11.8 ns. Thus, bivalent negatively charged monomer of the drug can be encapsulated into polymer/protein complexes, and drug release can be controlled by affecting electrostatic interactions within the complex.

Sample	**pH**	τ_1 ns	τ_2 ns	τ_3 ns	τ_{AV} ns	f_1 %	f_2 %	f_3 %
PrP	7.5	15.2 ± 0.2	2.7 ± 0.2	0.6 ± 0.1	12.6	79	21	0
	11	14.0 ± 0.1			9.8	63	37	0
EO-DMA/ins/PrP	7.5	12.2 ± 0.3			5.1	25	45	30
	11	16.4 ± 0.4			5.2	24	37	39
EO-**Q**DMA/ins/PrP	7.5	12.5 ± 0.3			7.0	48	31	21
	11	11.8 ± 0.4			3.3	18	32	50

Table 1. Lifetimes, τ, and fractional amplitudes, f, calculated by fitting fluorescence decays, measured at excitation wavelength, λ_{ex}, 375 nm and emission λ_{em} 630 nm, with bi- or tri-exponential function using global fit (τ_2 and τ_3 are the global parameters in simultaneous fitting of all 6 decays.). τ_{AV} is the average lifetime, calculated as $\tau_{AV}=\sum_{i=1}^{n} f_i\,\tau_i/100$, where n = 2 or 3.

Fig. 14 shows SAXS curves for the complexes after addition of the fluorophore. For this experiment, zinc (II) protoporphyrin-IX (ZnPrP) was used to enhance the contrast difference between DMA block and drug. Encapsulation of ZnPrP into EO-DMA/insulin complexes results in twofold decrease in forward scattering as well as fivefold decrease in the intensity of the correlation peak at q 0.11 Å^{-1} (Fig. 14a). Since the correlation peak corresponds to scattering from insulin molecules, ordered within the complex, the peak intensity decrease is related to variations in the contrasts within the complex and partial substitution of negatively charged insulin molecules to negatively charged bivalent ZnPrP. The latter is possible due to the competition of multivalent ions, that have comparable charge value and complete saturation of the complex due to the low degree of DMA ionization (44% of charged groups). The SLD of ZnPrP is lower than SLD of DMA, and, therefore, the decrease in scattering intensity at low q (below 0.1 Å^{-1}) for EO-

DMA/insulin/ZnPrP indicates loading of ZnPrP into the complexes. Similar effect was observed on SAXS curves of EO-DMA/insulin complexes with encapsulated PrP (Fig. S24). On the contrary, no effect on the SAXS profile for ZnPrP encapsulated into EO-QDMA/insulin complex was observed (see Fig. 14b) and the intensity of the correlation peak remains the same as for the complex itself. The SLD value of QDMA is similar to the one of ZnPrP, that explains why the scattering intensity at low q was not affected by drug encapsulation. At the same time, the intensity of the correlation peak remains the same, since EO-QDMA has 2 times higher degree of ionization, and, therefore, even at high insulin concentration there are enough charged QDMA groups to form complex with both insulin and ZnPrP. In this case, there is no competition between multivalent compounds. Hence, the detection of drug encapsulation could be accomplished by SAXS, revealing its effect on the internal structure of the complex.

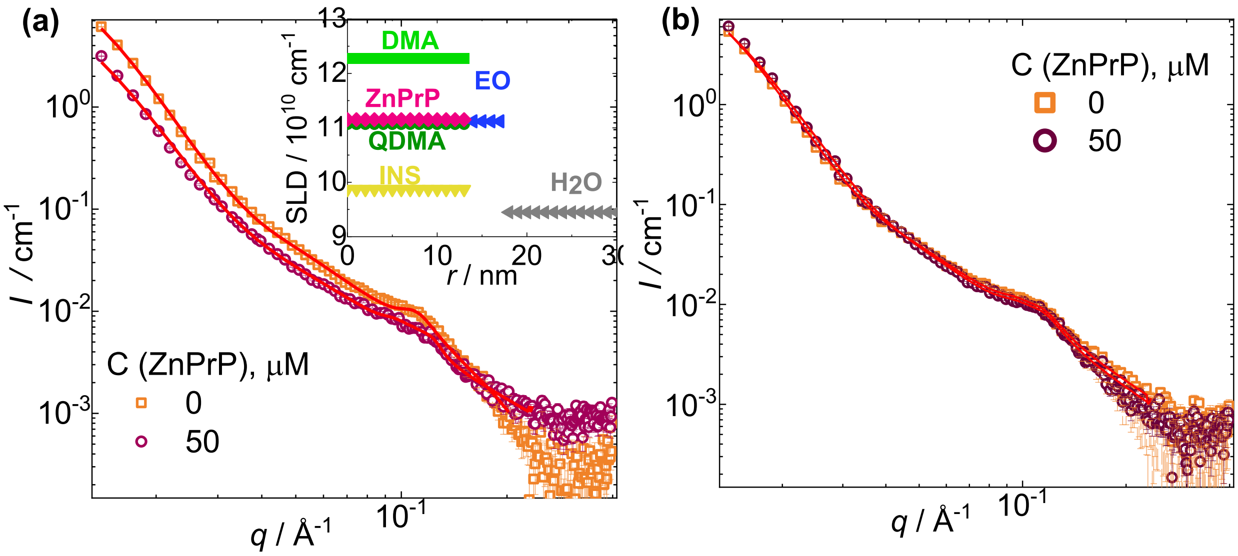

Fig. 14. SAXS profiles of insulin complexes with (a) weak EO-DMA, or (b) strong EO-QDMA and encapsulated ZnPrP at pH 7.5 in 50 mM NaCl H_2O. The polymer-to-insulin ratio for the experiment is 2.5. Inset: theoretical SLD of DMA, QDMA, EO blocks, insulin, and ZnPrP for X-rays.

CONCLUSION

Our study demonstrated the remarkable properties and potential applications of block copolymers containing weak or strong positively charged polyelectrolyte (PE) blocks in forming complexes with negatively charged insulin. We established that these complexes exhibit pH-responsiveness and disassemble at pH above 8 or below 5. This behavior makes them particularly suitable for drug delivery applications, as they can release their cargo in specific physiological environments, such as the acidic conditions of certain tissues with pH 4-5 or the alkaline environment of the gastrointestinal tract with pH 8-9. Furthermore, our research revealed the internal morphology of insulin complexes. We observed that insulin primarily exists in trimer form within these complexes, which is a significant finding considering that oligomeric form of insulin affects its biological activity. This implies that the complexes could potentially enhance the therapeutic efficacy of insulin. Moreover, we demonstrated that the arrangement of insulin aggregates within the complexes can be controlled by varying the ionic strength. This provides possibility to fine-tune the properties of the complexes and optimize their drug-loading capacity and release kinetics. The key advantages of these systems are reversibility of complex formation and controlled complex stability. Furthermore, the charge regulation can be modulated within the complex by adjusting the pH or the insulin-to-polymer ratio. This versatility opens opportunities for controlled drug release and sustainable delivery strategies.

In addition to insulin, we explored the encapsulation of bivalent negatively charged protoporphyrin-IX (PrP) within the complexes and pH induced release. The excess of PE positively charged groups in the complex allows for efficient encapsulation of PrP at physiological pH. The complexes release PrP upon particle disassembly triggered by pH increase. This highlights the broad applicability of the complexes for the delivery of negatively charged drugs other than insulin. Overall, the reversible complex formation, pH-responsiveness, and the ability to encapsulate and release various cargoes emphasize the potential of these complexes as controllable systems for the targeted delivery of therapeutic agents. Further investigations are needed to explore their in vivo performance and translate these results into clinical applications for improved disease treatments.

MATERIALS

Poly(ethylene oxide)-block-poly(N,N-dimethylaminoethyl methacrylate), EO_{204}-DMA_{40}, and poly(ethylene oxide)-block-poly(N,N-dimethylaminoethyl methacrylate)-d15, EO_{204}-DMA_{40}-d, were purchased from PolymerSource (PDI 1.10 and 1.19). Poly(ethylene oxide)-block-poly(N,N,N-trimethylammonioethyl methacrylate) EO_{204}-**Q**DMA_{40} and poly(ethylene oxide)-block-poly(N,N,N-trimethylammonioethyl methacrylate)-d18 EO_{204}-**Q**DMA_{40}-d were obtained by modification of EO-DMA and EO-DMA-d with methyl iodide (see chapter 1 in the Supporting Information). Human insulin was purchased from Sigma Aldrich. Protoporphyrin-IX (PrP) and zinc (II) protoporphyrin-IX (ZnPrP) were purchased from Sigma Aldrich (assay≥95%). Tris, NaCl, NaOH, HCl, NaOD, DCl, DMSO, DMSO-d6 were purchased from SigmaAldrich and used without purification.

Sample preparation. For samples with weak PE no buffer was used since both protein and polymer act as buffers at pH around 7.5, and all solutions were prepared in the presence of 50 mM NaCl. Insulin was dissolved in 50mM NaCl solution, small amount of sodium hydroxide was added to solution until insulin id fully dissolved, after which pH was adjusted to 7.5. EO-DMA or EO-DMA-d were dissolved in 50 mM NaCl, and pH was adjusted to 7.5 by hydrochloric acid. Stock solutions of polymer and insulin were mixed in ratios to adjust the total concentration of 5 g/l for polymer. For strong PE, polymer and insulin were prepared in the same way but in the presence of 13 mM Tris to keep constant pH. PrP and ZnPrP were dissolved in DMSO or deuterated DMSO-d6 (5 wt. %) and then added to aqueous solution of 13 mM Tris and 50 mM

NaCl at pH 11, so that PrP or ZnPrP concentration is 0.25 wt. %. The pH of PrP or ZnPrP solution was adjusted to 8 by HCl or DCl. The resulting concentration of PrP and ZnPrP in the polymer/insulin complexes was 25-50 µM, and since the concentration of DMSO in complexes was 0.03-0.055 %, we did not remove it by dialysis to avoid shifting an equilibrium between encapsulated and free PrP or ZnPrP.

METHODS

Potentiometric titration. Potentiometric titrations were performed using a Metrohm 888 Titrando Compact titrator equipped with a Metrohm LL Biotrode 3 mm glass electrode, a Pt1000 temperature sensor, a titration vessel for 1 ml, magnetic stirrer and Titrando Software. The standardized solutions of HCl and NaOH from Carl Roth GmbH (Karslruhe, Germany) were used to prepare 0.01 M stock solutions and kept under soda lime at least 24 hours before the measurements. The solutions of the polymers and insulin were prepared at concentrations of 5 g/l in 0.01 M standardized HCl. 2 ml of sample solution were weighed and then titrated by 0.01 M standardized NaOH using an automated dynamic pH titration method with signal drift 0.5 mV and waiting time 10 − 60 s. The stock solutions were kept under soda lime during the experiment to prevent contamination by CO_2. Blank titrations were performed before and after each polymer sample to estimate the concentration of CO_2 in solution. The average time of each experiment was ca. 90 min.

Isothermal titration calorimetry. The calorimetric experiments were performed with a MicroCal PEAQ ITC (Malvern Panalytical). The solution of 25 g/l insulin in 50 mM NaCl was titrated into 200 µl of 5 g/l EO-DMA or EO-QDMA solution in 50mM NaCl. A typical experiment consisted of 19 injections, 2 µL each. The time interval between injections was 2.5 min. Measurements were conducted at least 2 times with a fresh solution. Data were analyzed using a single-site binding model subtracting background enthalpies, whereas the stoichiometry coefficient, N, enthalpy, ΔH, and dissociation constant, K_D, are treated as adjustable parameters. The titration curves were analyzed and fitted using MicroCal PEAQ-ITC Analysis software.

Dynamic Light Scattering (DLS). DLS measurements were performed with a Litesizer (Anton Paar, Austria) at 20 °C at scattering angle 175°. DLS measurements for all systems were analyzed by fitting the normalized time autocorrelation function of the scattered light intensity using the constrained regularization algorithm (CONTIN). Each sample was filtered with PVDF 0.45µM syringe filter, and measured 3 times, each measurement consisted of 5 runs and run duration 30 seconds.

Electrophoretic Light Scattering (ELS). Zeta-potential measurements were performed with a Litesizer (Anton Paar, Austria) at 20 °C. The value of the electrophoretic mobility, μ, was averaged over three subsequent measurements, each of which consisting of 15 runs, and used to calculate the zeta-potential values, ζ, from the Henry equation in the Smoluchowski approximation, $\mu=\varepsilon\zeta/\eta$, where μ is the electrophoretic mobility, ε is the dielectric constant of the solvent, and η is the viscosity of solution.

Static Light Scattering (SLS). The static light scattering setup (ALV, Langen, Germany) consisted of a 22 mW He–Ne laser (λ 632.8 nm), an ALV CGS/8F goniometer, an ALV High QE APD detector, and an ALV 5004 multi-bit, multi-tau autocorrelator. The SLS measurements were performed at 20 °C and in scattering angle range from 70 to 150°. The copolymer mass concentration in the solution was C_{pol} 5 g L^{-1}. The samples were filtered using 0.45 µm Acrodisc PVDF membrane filters before the measurements.

Small-angle X-ray Scattering (SAXS). SAXS experiments were performed using "Ganesha-Air" instruments from SAXSLAB/XENOCS and Gallium Anode Low-Angle X-ray Instrument (GALAXI). The X-ray source of the laboratory-based "Ganesha-Air" system is a D2-MetalJet (Excillum) with a liquid metal anode operating at 70 kV and 3.57 mA with Ga−Kα radiation (wavelength λ = 0.134 nm). The beam is further focused with a focal length of 55 cm, using specially made X-ray optics (Xenocs) to provide a very narrow and intense beam at the sample position. Two pairs of scatterless slits are used to adjust the beam size depending on the detector distance. The data were acquired with a position-sensitive detector (PILATUS 300 K, Dectris). After calibration with silver behenate, the distance from the sample to the detector was set to 950 and 350 mm resulting in a q-range 0.13−6 nm^{-1}. Two four-segment slits, which are separated by 4 m distance, collimate the beam, and confine the size to about 0.7 × 0.7 mm^2. A third slit reduces the scattering from the edges of the second one. A sample-to-detector distance of 1285 mm calibrated using Bragg reflections from silver behenate resulting in a q-range of 0.09−4 nm^{-1} was used. All samples were sealed in glass capillaries of 2 mm inner diameter and measured in H_2O. Data analysis was done using the Python-based project Jscatter. SAXS curves were fitted using SASfit and SASview software.

Ultra Small-angle X-ray Scattering (USAXS). USAXS measurements were performed at SPring-8, Hyogo, Japan using a SAXS spectrometer installed on the BL19B2 beamline [28] at a sample-to-detector distances of 42 and 3 m. The X-ray wavelength was set to 0.69 Å and the covered q-range was q~ 0.0005–0.3 $Å^{-1}$. The exposure time for each sample was 5 min for 42 m and 0.5 min for 3 m. The PILATUS-2M detector collected the X-rays scattered from the samples. A sample transfer robot [28] able to transfer 120 samples was used for the SAXS measurements. The samples were inserted into quartz capillary tubes (Mark Tube; Hilgenberg GmbH, Germany) with a diameter of 2 mm. The solvent intensity was subtracted considering the transmission. The SAXS intensity was converted to absolute intensity using a secondary standard of glassy carbon. [29] All the SAXS measurements were performed at ambient temperature in H_2O and D_2O. USAXS curves were fitted using SASfit software.

Small-angle Neutron Scattering (SANS). SANS experiments for EO-DMA/insulin and EO-QDMA/insulin complexes with contrast variation were performed at the Australian National Science and Technology Organisation (ANSTO), Australia, on a Quokka beamline. [30] The instrument configuration of a wavelength λ = 6 Å, a wavelength spread ($\Delta\lambda/\lambda$) of 0.1, and sample-to-detector distances of 8 m and 1.3 m were selected to provide a q range of 0.007 $Å^{-1} < q < 0.4$ $Å^{-1}$. The q value is defined by $q = 4\pi\sin(\theta/2)/\lambda$, where θ and λ are the scattering angle and wavelength, respectively. The scattering intensity was reduced to an absolute scale using the direct beam flux method, the two measurements from the two detectors were merged into a single file, and the coherent scattering intensity was obtained after subtracting solvent scattering. Two-dimensional scattering images were corrected for detector sensitivity, sample transmission, empty cell scattering, and sample thickness, and then azimuthally averaged to produce the $I(q)$ vs. q plot following standard procedures.[31]

SANS measurements of the complexes at different pH and salt concentration were performed using TAIKAN on the BL15 beamline at the Material and Life Science Experimental Facility (MLF) in the Japan Proton Accelerator Research Complex (J-PARC).[32] The neutron wavelength was set to 0.8–7.8 Å. The sample-to-detector distance was 5.65 m. The samples were analyzed in a quartz cuvette of 2.0 mm thickness. SANS measurements were performed at 25 °C. The intensity of the scattering profile was converted to absolute intensity by subtraction with a profile of D_2O and standardization with a profile of glassy carbon.

SANS measurements for the complexes at different insulin concentration were performed at the Yellow Submarine diffractometer operating at the Budapest Neutron Center, Hungary.[33] The measurements were performed at ambient temperature of about 25 °C. The range of momentum transfer q was set to 0.07 - 4.5 nm^{-1}. Two configurations with sample-detector distances of 1.16 m and 5.26 m and mean neutron wavelengths of 0.42 nm and 0.97 nm were used to have access to the whole range of q. The raw data were corrected for sample transmission, scattering from the empty cell, and room background. Correction of the detector efficiency and conversion of the measured scattering to an absolute scale was performed by normalization to scattering from water. The corrected data were azimuthally averaged to produce the $I(q)$ vs. q plot following standard procedures. [31]

Hellma quartz cells 1 and 2 mm-thick were used for these experiments, which were performed in 50 mM sodium chloride in D_2O. The buffer was measured separately, and the scattering from the buffer was subtracted from the sample scattering. SANS curves were fitted using SASfit software with generalized Gaussian coil model for polymers or Sphere with attached Gaussian chains, extended Guinier law and Broad-Peak models for polymer/insulin complexes.

Ultra Small-angle Neutron Scattering (USANS). USANS experiments were performed using the small-angle neutron scattering spectrometer (SANS-J) installed at JRR-3 in JAEA, Tokai, Japan. Both pin-hole SANS (PSANS) and focusing SANS (F-SANS) were carried out in order to cover a wide q-range, where q is defined by $q = (4\pi/\lambda)\sin(\theta/2)$ (λ and θ being the wavelength and the scattering angle, respectively). The incident wavelength was 0.65 nm (wavelength resolution of 13%). In the case of PSANS, a two-dimensional ^{3}He position-sensitive detector collected the scattered neutrons from samples, and the sample-to-detector distances were 2.5 and 10.2 m. The size of source (A_0) and sample (A_s) aperture ware A_0 = 20 mm and A_s = 8 mm, respectively. Then, the covered q-range for PSANS is $4\times10^{-2} - 1.2$ nm^{-1}. On the other hand, F-SANS experiments were performed with using 70 biconcave MgF_2 lenses and a high-resolution scintillation detector consisting of a position-sensitive photomultiplier (diameter of 5 inch and spatial resolution of 0.5 mm) coupled with ZnS/6LiF scintillator (thickness of 0.2 mm), with A_0 = 3 mm and A_s = 15 mm, respectively. The sample-to-detector distance for F-SANS was fixed at

9.4 m. The covered q-range for F-SANS was realized to q $4\times10^{-3} - 5\times10^{-2}$ nm^{-1}. All measurements were performed at an ambient temperature (ca. 25 °C). After circular averaging, we subtracted for background scattering and converted the scattering intensity to the absolute intensity per sample volume by using a secondary standard of irradiated aluminum. [35]

Size exclusion chromatography (SEC). The chromatography experiment was conducted with the Knauer AZURA FPLC system with Superdex200 10/300 (Cytiva) column for insulin solution and Superdex75 10/300 (Cytiva) column for EO-DMA/insulin complexes, suitable for protein molecular weight within the range of 10 - 600 kDa. For each experiment, a solution volume of 200 µl was injected into the system, and a flow rate of 0.75 ml/min was set for elution. The measurements were performed under ambient temperature which was 21-22 °C. The signal from protein and the complexes was detected by UV-vis at wavelength, λ, 280 nm and multiangle light scattering (MALS) Wyatt DAWN HELEOS II.

Cryogenic transmission electron microscopy (cryo-TEM). For cryo-TEM experiment, 4 µl of sample solution were placed on a lacey carbon-coated copper grid at 20°C and 80% r.h., the excess of solution was blotted with filter paper in EMPG Leica GmbH grid plunger and rapidly immersed into liquid ethane. The specimen was inserted into a G910 multi-position specimen holder and transferred to a JEM 2200 FS EFTEM microscope (JEOL, Tokyo, Japan). Examinations were carried out at temperatures -179 °C. The microscope was operated at an acceleration voltage of 200 kV. Zero-loss filtered images were taken under reduced dose conditions (<10 000 e^-/nm^2). All images were recorded digitally by a bottom-mounted 16-bit CMOS camera system (TemCam-F216, TVIPS, Munich, Germany). All measurements were taken with intensity below 15 000 to avoid any saturation of the gray values. Images have been taken with EMenu 4.0 image acquisition program (TVIPS, Munich, Germany) and processed, particularly using band pass filter and improving brightness and contrast, with the free digital imaging processing system Image J. [34]

UV-vis spectroscopy. UV-vis spectra were measured using UV-2450 Spectrophotometer (Shimadzu) in 1 cm quartz cuvettes.

Fluorescence spectroscopy. Fluorescence emission and excitation spectra were measured using FS5 spectrophotometer (Edinburgh Instruments). The excitation spectra were measured in the wavelength range 300 – 600 nm at emission wavelength, λ_{em}, 630nm. The excitation spectra were measured in the wavelength range 550-750 nm at excitation wavelength, λ_{ex}, 375 nm.

Time-resolved fluorescence experiments were performed using FluoroTime 200 spectrometer (PicoQuant) based on a picoHarp300 time-correlated single photon counting unit using a pulsed diode laser (LDH-P-C-375B; λ=375nm; pulse width < 60 ps) at a repetition rate of 20 MHz. Emission decays were measured at excitation wavelength 375 nm and emission wavelength of 630 nm in a time window of 50 ns. Fluorescence decays were fitted by iterative reconvolution of the instrument response function with exponential model functions in PicoQuant FluoroFit software applying double or triple exponential functions with reconvolution using global fit (see section S6.3 in Supporting Information). All measurements were performed in 1 cm quartz cuvettes. Samples were measured at polymer concentration 5 g/l, insulin concentration 1 g/l to ensure excess of positively charged groups in the complexes and high sample transparency, and PrP concentration 25 μM.

ACKNOWLEDGEMENT

This paper is dedicated to the memory of Dr. Marie-Sousai Appavou, who unexpectedly passed away in September 2023. His significant contribution to electron microscopy holds profound importance for us.

The neutron experiment at the Materials and Life Science Experimental Facility of the J-PARC, BL15 TAIKAN beamline, was performed under a user program (Proposal No. 2022A0356). The research was undertaken on the Quokka beamline at the Australian Synchrotron, part of ANSTO (proposal No. P14494). The USANS experiment on SANS-J beamline at the JRR3 was performed under a user program (proposal No. 636). The SANS research for EO-DMA/insulin and EO-QDMA/insulin complexes was undertaken on the YS-SANS beamline at the BNC (proposal No. BNC-LENS-672). Atomic Force Microscopy (AFM) measurements were performed at the thin film laboratory operated by the JCNS at the Heinz Maier-Leibnitz Zentrum (MLZ), Garching, Germany. The authors are thankful to Dr. Pavlik Lettinga for his assistance with fluorescence experiments, Dr. Margarita Kruteva for the help with SAXS data analysis and Dr. Anthony Duff for the help with the lab equipment for sample preparation.

CONTRIBUTIONS

AM, AR and SF: design and conceptualization of research. AM and TG: fluorescence spectroscopy measurements and data analysis. MSA and BF: conducting cryo-TEM experiment. AM, KS and JA: chemical modification of polymers. MD: conducting SAXS measurements. AM and SM: conducting ITC measurements and data analysis. SW: supervision, resources, and data curation of ITC experiments. HI, HN, KW, LA and AL: conducting SANS experiments and primary data analysis. AM and AR: SANS and SAXS fitting. KI: conducting USAXS measurements and primary data analysis. AM and JJK: conducting SEC measurements and data analysis.

REFERENCES

[1] R. Pola, V. Král, S.K. Filippov, L. Kaberov, T. Etrych, I. Sieglová, J. Sedláček, M. Fábry, M. Pechar, Polymer Cancerostatics Targeted by Recombinant Antibody Fragments to GD2-Positive Tumor Cells, Biomacromolecules. 20 (2019) 412–421. https://doi.org/10.1021/acs.biomac.8b01616.

[2] A. Braunová, L. Kostka, L. Sivák, L. Cuchalová, Z. Hvězdová, R. Laga, S. Filippov, P. Černoch, M. Pechar, O. Janoušková, M. Šírová, T. Etrych, Tumor-targeted micelle-forming block copolymers for overcoming of multidrug resistance, J. Control. Release. 245 (2017) 41–51. https://doi.org/10.1016/j.jconrel.2016.11.020.

[3] R. Laga, O. Janoušková, K. Ulbrich, R. Pola, J. Blažková, S.K. Filippov, T. Etrych, M. Pechar, Thermoresponsive Polymer Micelles as Potential Nanosized Cancerostatics, Biomacromolecules. 16 (2015) 2493–2505. https://doi.org/10.1021/acs.biomac.5b00764.

[4] M. Skodova, M. Hruby, S.K. Filippov, G. Karlsson, H. Mackova, M. Spirkova, D. Kankova, M. Steinhart, P. Stepanek, K. Ulbrich, Novel Polymeric Nanoparticles Assembled by Metal Ion Addition, Macromol. Chem. Phys. 212 (2011) 2339–2348. https://doi.org/10.1002/macp.201100431.

[5] B.D. Ulery, L.S. Nair, C.T. Laurencin, Biomedical applications of biodegradable polymers, J. Polym. Sci. Part B Polym. Phys. 49 (2011) 832–864. https://doi.org/10.1002/polb.22259.

[6] M. Yanez Arteta, T. Kjellman, S. Bartesaghi, S. Wallin, X. Wu, A.J. Kvist, A. Dabkowska, N. Székely, A. Radulescu, J. Bergenholtz, L. Lindfors, Successful reprogramming of cellular protein production through mRNA delivered by functionalized lipid nanoparticles, Proc. Natl. Acad. Sci. 115 (2018). https://doi.org/10.1073/pnas.1720542115.

[7] N. Davies, D. Hovdal, N. Edmunds, P. Nordberg, A. Dahlén, A. Dabkowska, M.Y. Arteta, A. Radulescu, T. Kjellman, A. Höijer, F. Seeliger, E. Holmedal, E. Andihn, N. Bergenhem, A.-S. Sandinge, C. Johansson, L. Hultin, M. Johansson, J. Lindqvist, L. Björsson, Y. Jing, S. Bartesaghi, L. Lindfors, S. Andersson, Functionalized lipid nanoparticles for subcutaneous administration of mRNA to achieve systemic exposures of a therapeutic protein, Mol. Ther. - Nucleic Acids. 24 (2021) 369–384. https://doi.org/10.1016/j.omtn.2021.03.008.

[8] F. Sebastiani, M. Yanez Arteta, M. Lerche, L. Porcar, C. Lang, R.A. Bragg, C.S. Elmore, V.R. Krishnamurthy, R.A. Russell, T. Darwish, H. Pichler, S. Waldie, M. Moulin, M. Haertlein, V.T. Forsyth, L. Lindfors, M. Cárdenas, Apolipoprotein E Binding Drives Structural and Compositional Rearrangement of mRNA-Containing Lipid Nanoparticles, ACS Nano. 15 (2021) 6709–6722. https://doi.org/10.1021/acsnano.0c10064.

[9] C. Siewert, H. Haas, T. Nawroth, A. Ziller, S.S. Nogueira, M.A. Schroer, C.E. Blanchet, D.I. Svergun, A. Radulescu, F. Bates, Y. Huesemann, M.P. Radsak, U. Sahin, P. Langguth, Investigation of charge ratio variation in mRNA – DEAE-dextran polyplex delivery systems, Biomaterials. 192 (2019) 612–620. https://doi.org/10.1016/j.biomaterials.2018.10.020.

[10] R. Solaro, F. Chiellini, A. Battisti, Targeted Delivery of Protein Drugs by Nanocarriers, Materials (Basel). 3 (2010) 1928–1980. https://doi.org/10.3390/ma3031928.

[11] A. Riabtseva, L.I. Kaberov, J. Kučka, A. Bogomolova, P. Stepanek, S.K. Filippov, M. Hruby, Polyelectrolyte pH-Responsive Protein-Containing Nanoparticles: The Physicochemical Supramolecular Approach, Langmuir. 33 (2017) 764–772. https://doi.org/10.1021/acs.langmuir.6b03778.

[12] A. Skandalis, A. Murmiliuk, M. Štěpánek, S. Pispas, Physicochemical Evaluation of Insulin Complexes with QPDMAEMA-b-PLMA-b-POEGMA Cationic Amphiphlic Triblock Terpolymer Micelles, Polymers (Basel). 12 (2020) 309. https://doi.org/10.3390/polym12020309.

[13] N. Pippa, M. Karayianni, S. Pispas, C. Demetzos, Complexation of cationic-neutral block polyelectrolyte with insulin and in vitro release studies, Int. J. Pharm. 491 (2015) 136–143. https://doi.org/10.1016/j.ijpharm.2015.06.013.

[14] S. Mao, U. Bakowsky, A. Jintapattanakit, T. Kissel, Self-Assembled Polyelectrolyte

Nanocomplexes between Chitosan Derivatives and Insulin, J. Pharm. Sci. 95 (2006) 1035–1048. https://doi.org/10.1002/jps.20520.

[15] A.K. Attri, C. Fernández, A.P. Minton, pH-dependent self-association of zinc-free insulin characterized by concentration-gradient static light scattering, Biophys. Chem. 148 (2010) 28–33. https://doi.org/10.1016/j.bpc.2010.02.002.

[16] R.N. Farías, A.E. López Viñals, E. Posse, R.D. Morero, Relationship between isoelectric point of native and chemically modified insulin and liposomal fusion, Biochem. J. 264 (1989) 285–287. https://doi.org/10.1042/bj2640285.

[17] V.H. Le, R. Buscaglia, J.B. Chaires, E.A. Lewis, Modeling complex equilibria in isothermal titration calorimetry experiments: Thermodynamic parameters estimation for a three-binding-site model, Anal. Biochem. 434 (2013) 233–241. https://doi.org/10.1016/j.ab.2012.11.030.

[18] J. Gummel, F. Cousin, F. Boué, Counterions Release from Electrostatic Complexes of Polyelectrolytes and Proteins of Opposite Charge: A Direct Measurement, J. Am. Chem. Soc. 129 (2007) 5806–5807. https://doi.org/10.1021/ja070414t.

[19] K. Henzler, B. Haupt, K. Lauterbach, A. Wittemann, O. Borisov, M. Ballauff, Adsorption of β-Lactoglobulin on Spherical Polyelectrolyte Brushes: Direct Proof of Counterion Release by Isothermal Titration Calorimetry, J. Am. Chem. Soc. 132 (2010) 3159–3163. https://doi.org/10.1021/ja909938c.

[20] J.M. Fay, A. V. Kabanov, Interpolyelectrolyte Complexes as an Emerging Technology for Pharmaceutical Delivery of Polypeptides, Rev. Adv. Chem. 12 (2022) 137–162. https://doi.org/10.1134/S2634827622600177.

[21] C. Branca, A. Faraone, S. Magazù, G. Maisano, P. Migliardo, A. Triolo, R. Triolo, V. Villari, Anomalous conformational properties of PEO in H 2 O and D 2 O by SANS, PCS and Raman scattering, J. Appl. Crystallogr. 33 (2000) 709–713. https://doi.org/10.1107/S0021889899013242.

[22] B. Hammouda, D.L. Ho, S. Kline, Insight into clustering in poly(ethylene oxide) solutions, Macromolecules. 37 (2004) 6932–6937. https://doi.org/10.1021/ma049623d.

[23] B. Hammouda, D. Ho, S. Kline, SANS from Poly(ethylene oxide)/Water Systems, Macromolecules. 35 (2002) 8578–8585. https://doi.org/10.1021/ma011657n.

[24] S. Jakobsen, K. Kristensen, F. Jensen, Electrostatic Potential of Insulin: Exploring the Limitations of Density Functional Theory and Force Field Methods, J. Chem. Theory Comput. 9 (2013) 3978–3985. https://doi.org/10.1021/ct400452f.

[25] L.M. Scolaro, M. Castriciano, A. Romeo, S. Patanè, E. Cefalì, M. Allegrini, Aggregation Behavior of Protoporphyrin IX in Aqueous Solutions: Clear Evidence of Vesicle Formation, J. Phys. Chem. B. 106 (2002) 2453–2459. https://doi.org/10.1021/jp013155h.

[26] A.. Savitski, E.. Vorobyova, I.. Berezin, N.. Ugarova, Acid—base properties of protoporphyrin IX; its dimethyl ester and heme solubilized on surfactant micelles: spectrophotometric and fluorometric titration, J. Colloid Interface Sci. 84 (1981) 175–181. https://doi.org/10.1016/0021-9797(81)90272-1.

[27] D.C.K. Codognato, F.S. Pena, E.R. dos Reis, A.P. Ramos, I.E. Borissevitch, Effects of serum albumin on the photophysical characteristics of synthetic and endogenous protoporphyrin IX, Brazilian J. Med. Biol. Res. 55 (2022). https://doi.org/10.1590/1414-431x2022e12272.

[28] K. Osaka, T. Matsumoto, Y. Taniguchi, D. Inoue, M. Sato, N. Sano, High-throughput and automated SAXS/USAXS experiment for industrial use at BL19B2 in SPring-8, in: 2016: p. 030003. https://doi.org/10.1063/1.4952826.

[29] F. Zhang, J. Ilavsky, G.G. Long, J.P.G. Quintana, A.J. Allen, P.R. Jemian, Glassy Carbon as an Absolute Intensity Calibration Standard for Small-Angle Scattering, Metall. Mater. Trans. A. 41 (2010) 1151–1158. https://doi.org/10.1007/s11661-009-9950-x.

[30] K. Wood, J.P. Mata, C.J. Garvey, C.-M. Wu, W.A. Hamilton, P. Abbeywick, D. Bartlett, F. Bartsch, P. Baxter, N. Booth, W. Brown, J. Christoforidis, D. Clowes, T. D’Adam, F. Darmann, M. Deura, S. Harrison, N. Hauser, G. Horton, D. Federici, F. Franceschini, P. Hanson, E. Imamovic, P. Imperia, M. Jones, S. Kennedy, S. Kim, T. Lam, W.T. Lee, M. Lesha, D. Mannicke, T. Noakes, S.R. Olsen, J.C. Osborn, D. Penny, M. Perry, S.A. Pullen, R.A. Robinson, J.C. Schulz, N. Xiong, E.P. Gilbert, QUOKKA, the pinhole small-angle neutron scattering instrument at the OPAL Research Reactor, Australia: design, performance, operation and scientific highlights, J. Appl. Crystallogr. 51 (2018) 294–314. https://doi.org/10.1107/S1600576718002534.

[31] S.R. Kline, Reduction and analysis of SANS and USANS data using IGOR Pro, J. Appl. Crystallogr. 39 (2006) 895–900. https://doi.org/10.1107/S0021889806035059.

[32] S. Takata, J. Suzuki, T. Shinohara, T. Oku, T. Tominaga, K. Ohishi, H. Iwase, T. Nakatani, Y. Inamura, T. Ito, K. Suzuya, K. Aizawa, M. Arai, T. Otomo, M. Sugiyama, The Design and q Resolution of the Small and Wide Angle Neutron Scattering Instrument (TAIKAN) in J-PARC, in: Proc. 2nd Int. Symp. Sci. J-PARC — Unlocking Myster. Life, Matter Universe —, Journal of the Physical Society of Japan, 2015. https://doi.org/10.7566/JPSCP.8.036020.

[33] L. Almásy, New Measurement Control Software on the Yellow Submarine SANS Instrument at the Budapest Neutron Centre, J. Surf. Investig. X-Ray, Synchrotron Neutron Tech. 15 (2021) 527–531. https://doi.org/10.1134/S1027451021030046.

[34] C.A. Schneider, W.S. Rasband, K.W. Eliceiri, NIH Image to ImageJ: 25 years of image analysis, Nat. Methods. 9 (2012) 671–675. https://doi.org/10.1038/nmeth.2089.

[35] T. Kumada, R. Motokawa, Y. Oba, H. Nakagawa, Y. Sekine, C. Micheau, Y. Ueda, T. Sugita, A. Birumachi, M. Sasaki, K. Hiroi, H. Iwase, Upgrade of the small-angle neutron scattering diffractometer SANS-J at JRR-3, J. Appl. Crystallogr. 56 (2023) 1776–1783. https://doi.org/10.1107/S1600576723009731.